Kirkpatrick, H.M., Moon, S., Yin, A., and Harrison, T.M., 2020, Impact of fault damage on eastern Tibet topography: Geology, v. 48, https://doi.org/10.1130/G48179.1

GSA Data Repository Items

A. Supplementary text
    - Geologic Background and Compiled Faults
    - Determination of Erosion Rates
    - Quantification of Topographic, Geologic, Climatic, and Ecologic Parameters
    - Quantification of Erosion Coefficients and Rate Constants
    - Statistical Analysis
    - Schmidt Hammer Measurements of Rock Strengths

B. Supplementary figures
    - Figure S1. Maps showing basins sampled in this study
    - Figure S2. Maps showing spatial variations of various factors in eastern Tibet
    - Figure S3. Maps showing basin averaged values of various factors in eastern Tibet
    - Figure S4. Relationships between erosion coefficients and the distance to major faults for varying basin groups
    - Figure S5. Relationships between erosion rate, k_{sn}, erosion coefficients, and distance to faults
    - Figure S6. Relationships between erosion coefficients and precipitation, NDVI, and PGA
    - Figure S7. Relationships between erosion coefficients from different model assumptions and distance to major faults
    - Figure S8. Relationships between erosion coefficients and distance to major faults for a subset of basins not significantly affected by the 2008 Wenchuan Earthquake

- Figure S9. Conceptual diagram of fault core and damage zones and an idealized topographic expression
- Figure S10. Maps of site locations for the Schmidt hammer measurements
- Figure S11. Ranges of Schmidt hammer *H*-values

C. Supplementary tables

- Table S1. Erosion rates and cosmogenic concentrations from previous studies
- Table S2. Erosion rates and cosmogenic concentrations measured in this study
- Table S3. Topographic, climatic, and ecologic variables and erosion coefficients for studied basins
- Table S4. RMSE (mm yr^{-1}) from relationships between erosion rates and topographic metrics
- Table S5. Percentages of different rock types within studied basins
- Table S6. Number of basins dominated by each lithologic type
- Table S7. Correlation between erosion coefficients and potential controls
- Table S8. Ranges of erosion coefficients for categories of basins grouped by drainage area, dominant lithologies, and distance to major faults
- Table S9. *F*-test and *t*-test results
- Table S10. Schmidt hammer *H*-values

A. Supplementary Text

Geologic Background and Compiled Faults

In the northeastern part of the Tibetan Plateau near the Longmen Shan region, Triassic and Paleozoic siliciclastic and carbonate strata dominate (Kirby and Ouimet, 2011; Hartmann and Moosdorf, 2012; Tian et al., 2018). Precambrian basement rock and Mesozoic plutons are exposed in the hanging walls of thrust faults as gneiss domes or metamorphic massifs in the frontal Longmen Shan region (Tian et al., 2018). The dominant rock types in the Min Shan range to the north are Triassic and Paleozoic sedimentary rocks (Kirby and Ouimet, 2011). In addition, small areas (a few km^2) of volcanic rocks, plutonic rocks, and unconsolidated surficial deposits are scattered across eastern Tibet (Hartmann and Moosdorf, 2012). Compared to the dominance of sedimentary rocks to the north, the southwestern part of our study area has a higher proportion of metamorphic and plutonic rocks including the Gongga and Luding granites (Hartmann and Moosdorf, 2012; Zhang et al., 2017).

To examine the impact of fault damage on erosion, we compiled faults and fault systems located in eastern Tibet. Because detailed, local-scale fault maps are not consistently available throughout our study area, we only consider regional-scale (>50 km in length) faults and fault systems (hereafter, major faults) systematically documented by previous studies (Burchfiel et al., 1998; Chen and Wilson, 1996; Kirby et al., 2002; Burchfiel and Chen, 2012; Yan et al., 2011; Yan et al., 2018). In addition, we consider both inactive and active faults because damage zones of both active and inactive faults could have an influence on shaping present-day topography. Most major faults mapped in this study area are active faults based on current literature (86% in total length). Only a few inactive structures are present in the frontal Longmen Shan, which include (1) the low-angle shear zones separating the basement rocks from the sedimentary sequence, and (2) narrow klippen structures duplicated by the Cenozoic thrusts and placing Late Paleozoic strata over Jurassic strata (Chen and Wilson, 1996; Kirby et al., 2002; Yan et al., 2011).

We use fault maps from Burchfiel et al. (1995), Chen and Wilson (1996), and Kirby et al. (2002) as base maps and extend our compilation to include faults from Pan et al. (2004), Wang et al. (2012), Ren et al. (2013a, b), Long et al. (2015), Ansberque et al. (2015), Zhang et al. (2015), Chavalier et al. (2016), Ren et al. (2018), Yan et al., (2011) and Yan et al. (2018). The faults and fault systems considered in this study include the Beichuan-Yingxiu fault (B.-Y.F.), the Guanxian-Anxian fault (G.-A.F), the Huya fault (H.F.), the Jiulong fault system (J.F.S.), the nappes and klippen belts near the frontal Longmen Shan (n.k.), the Kunlun fault system (K.F.), the Litang fault system (L.F.), the Longriba fault system (L.F.S.), the Maerkang fault (Ma.F.), the Minjiang fault (Mi.F.), the Maowen fault (Mao.F.), the Muli fault (Mu.F.), the Qingchuan-Pingwu fault (Q.-P.F.), the Xianshuihe fault system (X.F.S.), and the Xueshan fault (XS.F).

Faults that have been active during the Quaternary (hereafter, active faults) and for which we have records of historic or recent seismic activity are discussed below. The Beichuan, Wenchuan, and Pengguan fault zones near the frontal Longmen Shan region have experienced several $M_w > 6.5$ earthquakes over the last 50 years, including the 2008 M_w 7.9 Wenchuan earthquake (Chen et al., 1994; Xu et al., 2017). To the north, the Min Shan region also has several active faults including the north-striking Min Jiang fault (1933 M_w 7.38 earthquake; International Seismology Centre), the east-striking Xueshan fault which was possibly reactivated from a Mesozoic structure (Kirby et al., 2000), the northwest-striking Huya fault, and the northeast-striking Qingchuan fault (Chen et al., 1994; Burchfiel et al., 1995; Taylor and Yin, 2009; Xu et al., 2017). Four $M_w \geq 6.5$ earthquakes have occurred along the Huya fault in the last ~50 years: three in 1976 (Chen et al., 1994) and one, the M_w 6.5 Jiuzhaigou earthquake, in 2017 (Xu et al., 2017; IRIS, www.iris.edu). North of the Longmen Shan, a M_w 6.1 earthquake occurred along the Maerkang fault on September 22, 1989 indicating that this fault is also active

(IRIS, www.iris.edu). There is no record of historic earthquakes occurring along faults in the Longriba fault system (the Longriqu fault and the Maoergai fault), but Ren et al. (2013a, 2013b) determined from trenching, landform mapping, radiocarbon dating, and OSL dating that the Maoergai fault (southern) last ruptured about 5170 ± 80 years ago and the Longriqu fault (northern) last ruptured about 5080 ± 90 years ago. The Daxue Shan region in the southern part of our study area contains the Xianshuihe fault system consisting of four segments: Ganzi, Xianshuihe, Anninghe, and Zemuhe-Xiajiang (Allen et al., 1991; e.g. Zhang et al., 2017) along which several $M_w < 6.5$ earthquakes occurred in the last 50 years (IRIS, www.iris.edu). The Litang fault, south of the Xianshuihe fault, has hosted several $M_w > 5$ earthquakes since 1976 (IRIS, www.iris.edu). The spatial distributions of active and inactive faults are shown in brown solid lines and blue dashed lines in Fig. 1, respectively.

Determination of Erosion Rates

In situ production of cosmogenic radionuclides, such as ^{10}Be and ^{26}Al, mostly occurs within 1-2 m of Earth's surface and decreases exponentially with depth (Lal, 1991; Bierman and Steig, 1996; Granger et al., 1996; Balco et al., 2008; Dunai, 2010). We first compiled erosion rates using ^{10}Be isotopes from previous studies (Ouimet et al., 2009; Godard et al., 2010; Ansberque et al., 2015). Following the approaches of previous studies (Ouimet et al., 2009, Kirby and Ouimet, 2011, Scherler et al., 2017), we excluded 11 basins which are glaciated (wbo549, wbo550, and wbo633) and affected by landslide derived sediments (wbo523, wbo637, and wbo639). This is because basins affected by landslides and glaciers likely have biased ^{10}Be-derived erosion rates due to a significant input of sediment with low ^{10}Be concentrations (Hallet and Hunter, 1996; Niemi et al., 2005). In addition, we excluded basins with areas larger than

6000 km^2 due to potentially inconsistent sediment delivery over time (LM254, LM261, LM263, SC049, and SC086). Previous studies have also removed samples with large basin areas (Kirby and Ouimet, 2011; Scherler et al., 2017). We used averaged erosion rates for duplicate samples from 3 basins (LM253 and SC082; wbo610s and wbo610q; wbo624s and wbo624q). We only used basin-averaged erosion rates of the original sampled basins and did not recalculate erosion rates for partial areas of nested basins. This resulted in a total of 100 erosion rate measurements compiled from previous studies (Ouimet et al., 2009; Godard et al., 2010; Ansberque et al., 2015).

We measured millennial erosion rates using ^{10}Be isotopes for 11 basins from the Min Shan. We collected sand samples from nine basins in the Fu Jiang catchment (ET01-ET06, ET08-ET10), one basin from the Min Jiang catchment (ET12), and one basin draining the Bailong He catchment (ET11) in September 2016 (Fig. S1). Our collected samples were sieved at UCLA, and the 250-500 μm size fraction was used for measurements. Quartz was purified by a series of chemical leaching steps using concentrated HNO_3 and an ~1% HNO_3 and ~1% HF mixture with DI water, and samples were separated using a magnetic separator and LST at PRIME Lab, Purdue University. A total of 1.5 – 23.3 g quartz was dissolved after adding 0.235-0.261 mg of ^{9}Be carrier. Be fractions were extracted using ion-exchange chromatography. The ^{10}Be/^{9}Be ratios were measured by Accelerator Mass Spectrometry at PRIME Lab, Purdue University based on the calibration of Nishiizumi et al. (2007) (Table S2). Two full process blanks for ^{10}Be/^{9}Be were measured as $(1.1\text{-}1.5) \times 10^{-15}$, and the averaged ^{10}Be atoms per mg of ^{9}Be carrier was 85,408. The total ^{10}Be atoms in the blanks include ^{10}Be from the carrier and additions from chemical and measurement processes. ^{10}Be atoms from the carrier were subtracted from measured total concentrations to calculate carrier-corrected ^{10}Be atoms per g of quartz.

Topographic metrics required for erosion calculations including topographic shielding, mean latitude, mean longitude, and mean elevation were calculated via TopoToolbox in Matlab (Schwanghart and Scherler, 2014). These values along with measured concentrations of ^{10}Be and an assumed rock density of 2.7 g cm^{-3} were then used to compute erosion rates assuming the Lal (1991)-Stone (2000) time-dependent production model from the CRONUS online calculator version 3 (Lifton et al., 2014; Balco et al., 2008) (Table S1 and S2). The recalculation of erosion rates was needed to standardize data for the same ^{10}Be half-life (Nishiizumi et al., 2007), production rate scaling schemes (Balco et al., 2008), rock density, and topographic shielding. On average, the newly calculated erosion rates are ~0.08 mm yr^{-1} (0.07 mm yr^{-1}, 1 s.d.) less than the previously published values but show a strong linear correlation (R^2 = 0.99) with previous measurements.

Erosion rates from 11 basins measured in this study vary from 0.24 ± 0.06 mm yr^{-1} to 0.76 ± 0.08 mm yr^{-1}. The highest erosion rates in the Min Shan region, ET06 (0.62 ± 0.08 mm yr^{-1}), ET09 (0.76 ± 0.08 mm yr^{-1}), and ET10 (0.53 ± 0.08 mm yr^{-1}), correspond to basins near the Huya fault (Fig. 1A; Fig. S1). The lowest erosion rate (ET12, 0.24±0.06 mm yr^{-1}) presented here corresponds to sediment collected from the headwaters of rivers that flow into the Longmen Shan. ET11 (0.31 ± 0.03 mm yr^{-1}), which is partially on the low relief portion of the plateau and has an erosion rate similar to those on the plateau, was collected in a tributary to a river north of the Fu Jiang (Bailong Jiang).

Quantification of Topographic, Geologic, Climatic, and Ecologic Parameters

We calculated topographic metrics, including slope, local relief, and channel steepness, for each basin using ArcGIS and TopoToolbox in Matlab (Schwanghart and Scherler, 2014) (Table S3). We primarily used the 90 m void filled SRTM DEM (https://earthexplorer.usgs.gov/). For portions of basins where the 90 m void filled STRM DEM did not have data, we used the DEM provided by de Ferranti (2018) (~6% of studied basins). Slope is calculated along the steepest descent direction in an 8-cell neighborhood, and local relief is calculated as the elevation difference between the highest and lowest elevations within a 1 km radius circular window. For channel steepness (k_{sn}), we extracted channel points with drainage areas larger than 1 km^2 and calculated basin-averaged k_{sn} through two methods by (1) the integral method based on χ (Perron & Royden, 2013; Scherler et al., 2017) and (2) averages of channel steepness that are calculated as normalized channel slope by drainage area (Wobus et al., 2006; Ouimet et al., 2009; Kirby and Ouimet, 2011; Scherler et al., 2017). In the integral method, channel steepness k_s [$L^{2\theta}$] is calculated from the fit between elevation z and χ (Perron and Royden, 2013) as:

$$z(x) = z(x_b) + \left(\frac{k_s}{A_0{}^{\theta}}\right)\chi \qquad (1)$$

where $\chi = \int_{x_b}^{x} \left(\frac{A_0}{A(x)}\right)^{\theta} dx$, x is horizontal distance [L], b is the base level, and A_0 is a reference drainage area [L^2; A_0 = 1 km^2]. We calculated normalized channel steepness (k_{sn}) assuming a reference concavity θ of 0.45, which is consistent with previous studies of this area (Ouimet et al., 2009; Kirby and Ouimet, 2011; Scherler et al., 2017). Both the integral method and values obtained from averaging channel points show comparable results to each other (R^2 = 0.97), and are similar to calculations in Scherler et al. (2017). Following Scherler et al. (2017), we used k_{sn} from the integral method based on χ for calculating erosion coefficients.

Basin-averaged slopes range from 0.07 (± 0.05) to 0.89 (± 0.42), and basin-averaged local relief range from 130 (± 88) to 1268 (± 173) m. Basin-averaged channel steepness, k_{sn}, from the integral method range from 14 (1 s.e., ± 0.1) to 465 (1 s.e., ± 10) $m^{0.9}$ (Table S3; Fig. 2). We quantified percent areas of lithologies for each basin based on a lithologic map by Hartmann and Moosdorf (2012). We defined 7 rock classifications (metamorphic rocks, plutonic rocks, carbonate rocks, mixed composition sedimentary rocks that include both siliciclastic and carbonate sedimentary rocks (hereafter, mixed composition sedimentary rocks), siliciclastic sedimentary rocks, unconsolidated sedimentary rocks, and volcanic and pyroclastic rocks). We quantified areal percentages of each lithologic group for our studied basins (Table S5). Most basins consist of multiple lithologic groups. The number of basins that are dominated by (>50% in area) or composed entirely of a single lithologic group are listed in Table S6. To provide statistical significance, we focus on small basins with areas (A) < 200 km^2 dominated by three dominant single lithologic groups (i.e., plutonic rocks, mixed composition sedimentary rocks, and siliciclastic sedimentary rocks) that have more than 10 basins. We use an area of 200 km^2 as the largest basin size for our "small basin" group following Ouimet et al. (2009) who used small catchments from the eastern margin of the Tibetan Plateau.

To examine various controlling factors on erosion coefficients, we quantified basin-averaged values of fault distance, mean annual precipitation (MAP), normalized difference vegetation index ($NDVI$), and peak ground acceleration from the 2008 Wenchuan earthquake (PGA) by averaging corresponding values from all pixels within drainage areas. To do this, we first quantified the distance to faults as the linear horizontal distance between each pixel to its closest point among the major faults (Fig. 1). We quantified the distance to major faults (D_{mf}) considering both active and inactive faults and the distance to major active faults considering only active faults. We quantified mean annual precipitation rates based on the Tropical Rainfall Measuring Mission (*TRMM*) precipitation measurements averaged from 1998 to 2008 (Bookhagen et al., 2010). In addition, we quantified basin-averaged *NDVI*, a measure of vegetation amount and health, as,

$$NDVI = \frac{(NIR-VIS)}{(NIR+VIS)} \tag{2}$$

where NIR and VIS stand for the surface reflectance measurements of near-infrared and visible (red) bands, respectively. *NDVI* ranges from -1 to +1. Areas with low or negative *NDVI* indicate no or sparse vegetation while those with high *NDVI*, or values close to 1, indicate dense and healthy vegetation. We used a 250 m-resolution *NDVI* derived from a 16-day period (07/28/2019 to 08/12/2019 without clouds), which was downloaded from the Terra Moderate Resolution Imaging Spectroradiometer (MODIS) Vegetation Indices (MOD13Q1) Version 6 (Data accessed on 08/29/19; Didan et al., 2015).

Lastly, we quantified the basin-averaged peak ground acceleration (*PGA*) that was simulated for the 2008 M_w 7.9 Wenchuan earthquake that ruptured ~270 km of the frontal Longmen Shan fault system. A previous study by Li et al. (2017) showed that earthquake-induced landslides from large magnitude earthquakes similar to the 2008 Wenchuan earthquake contribute significantly to the long-term denudation rates inferred from cosmogenic nuclides and low temperature thermochronology. In this case, seismic shaking from large earthquakes can enhance erosion by generating coseismic landslides and influence erosion coefficients. To examine this, we quantified the basin-averaged *PGA* based on simulated *PGA* from USGS ShakeMap Atlas v4 (Data accessed on 06/08/20). Basin-averaged *PGA* varies from 0.02 g to 0.92 g. For reference, *PGA* values < 0.0017 g, 0.0017-0.014 g, 0.014-0.039 g, 0.039-0.092 g, 0.092-0.18 g, 0.18-0.34 g, 0.34-0.65 g, and 0.65-1.24 g correspond to a perceived shaking of not felt, weak, light, moderate, strong, very strong, severe, and violent, respectively.

In addition, West et al., (2014) showed that input from earthquake-induce landslides from the 2008 M_w 7.9 Wenchuan earthquake diluted ^{10}Be concentrations in quartz, especially in areas with high *PGA* and extensive coseismic landslides (> ~0.3 % of the upstream catchment area affected by landslides). However, in areas with low landslide occurrences, there were no systematic changes in ^{10}Be concentration in quartz. Significant inputs from earthquake-induced landslides can result in increased ^{10}Be-derived erosion rates which may not be representative of long-term millennial erosion rates. Most coseismic landslides from the 2008 Wenchuan earthquake occurred within ~30 km of the Beichuan-Yingxiu fault surface rupture and have a *PGA* greater than 0.2 g (Xu et al., 2014; Li et al., 2017). Thus, we performed sensitivity analyses using (1) basins sampled before the 2008 Wenchuan earthquake and (2) basins sampled before the 2008 Wenchuan earthquake or sampled outside of the severe shaking range after the 2008 Wenchuan earthquake (i.e. $PGA < 0.34$ g). This follows a similar criterion to what is used in Ansberque et al. (2015).

Quantification of Erosion Coefficients and Rate Constants

For the analyses in the main text, we quantified erosion coefficient, K, from the linear relationship between erosion rate, E, and normalized channel steepness calculated from the integral method, k_{sn}. We calculated the root-mean-square-errors (RMSE) to examine the goodness of the fits of linear and nonlinear (exponential or power-law) models between E and k_{sn}. RMSE is calculated by taking the square root of the sum of squared errors (SSE) divided by degrees of freedom (df = number of data points - number of parameters). RMSE values from linear and nonlinear models are similar between erosion rate and various topographic metrics including channel steepness, slope, and local relief, when looking both at all basins and only small basins with $A < 200$ km^2 (Table S4). Since the linear and nonlinear models produce comparable results, we calculated the erosion coefficient, *K,* assuming a linear model ($n = 1$) without an intercept (eq. 3 in the main text). The use of $n = 1$ is consistent with the approaches of previous studies in this study area (Ouimet et al. 2009; Kirby and Ouimet, 2011, Scherler et al., 2017). To examine the differences, we also calculated erosion coefficient, K_{nl}, assuming the best-fit, nonlinear relationship between erosion rate and channel steepness (power-law model, $E = K_{nl} \cdot k_{sn}{}^{n}$; $n = 0.49$).

We also examined erosion coefficients calculated based on different assumptions of river incision models or rate constants calculated for different topographic metrics (Table S3). First, we calculated the erosion coefficients, K_{sp} and K_{ss}, using discharge instead of drainage area and determined the expected exponents based on stream power or shear stress incision models, respectively (e.g., Whipple et al., 1999, Finlayson et al., 2002). The erosion rates are related to controls as,

$$E = K_i \, (Q^{a_i} S^{b_i})^{n_i} \qquad (3)$$

where E is erosion rate [L t^{-1}], Q is stream discharge [L^3 t^{-1}], S is slope [dimensionless], and a and b are constants that differ depending on stream power ($i = sp$) or shear stress ($i = ss$) based erosion models, and n_i is an empirical constant. For the stream power-based erosion model, $a = 1/2$ and $b = 1$. For the shear stress-based erosion model, $a = 1/3$ and $b = 2/3$. We calculated the spatial distribution of Q by integrating mean annual precipitation of upstream grid cells assuming infiltration or evapotranspiration are negligible or proportional to precipitation. We acknowledge that this assumption may not be applicable to certain areas. However, due to the lack of a high-resolution discharge dataset, this assumption is necessary to quantify the spatial distribution of Q. Based on relationships between basin-averaged erosion rates and basin-averaged values of discharge as well as slope, we determine n_{sp} and n_{ss}. There are comparable RMSE from nonlinear power-law and linear models (Table S4). Assuming best-fit, power-law exponents of n_{sp} =0.50 and n_{ss} =0.63, we calculated K_{sp} and K_{ss}. Unlike K, erosion coefficients of K_{sp} and K_{ss} are less affected by the spatial variations of precipitation or discharge.

Then, we calculated the rate constants from relationships between basin-averaged erosion rates and topographic metrics of hillslope gradient and local relief. Previous studies have also shown empirical relationships between erosion rate and hillslope gradient or local relief (Montgomery and Brandon, 2002, Portenga and Bierman, 2011). Topographic metrics of both hillslope gradient and local relief have comparable RMSE from nonlinear power-law and linear models (Table S4). Following the previous studies which showed non-linear relationships between erosion rate and hillslope gradient or local relief (Ouimet et al., 2009; Kirby and Ouimet, 2011), we determined the best-fit, nonlinear power-law relationship between erosion rates E and hillslope gradient ($E = 0.46 \times S^{1.44}$; RMSE = 0.108 mm yr^{-1}) and local relief ($E = 6.8\times10^{-5}\times LR^{1.2}$, RMSE = 0.107 mm yr^{-1}). Using the power-law exponents of n = 1.44 and n = 1.20, we quantified rate constants for hillslope gradient (K_{slp}) and local relief (K_{lr}) for each basin, respectively.

Statistical Analysis

First, we examined how K, K_{nl}, K_{ss}, K_{sp}, K_{slp}, and K_{lr}, vary with potential controls including distance to major faults (D_{mf}), distance to major active faults, mean annual precipitation rates, *NDVI*, and *PGA* (Table S7). We examined five groups including all basins (n

= 111), small basins with $A < 200$ km^2 ($n = 95$), and small basins dominated by siliciclastic sedimentary rocks ($n = 56$), mixed composition sedimentary rocks ($n = 18$), and plutonic rocks ($n = 11$).

All rate constants (K, K_{nl}, K_{ss}, K_{sp}, K_{slp}, and K_{lr}) show statistically significant (p-value < 0.05), inverse relationships with (1) distance to major faults and (2) distance to major active faults for all basins, small basins, and small basins dominated by siliciclastic sedimentary rocks. This is also true for small basins composed of 100% siliciclastic sedimentary rocks ($n = 33$). For small basins dominated by mixed composition sedimentary rocks, K shows statistically significant inverse relationships with distance to major faults and distance to major active faults. The K from small basins dominated by plutonic rocks has a stronger positive correlation with precipitation ($R = 0.69$, p-value = 0.02) than distance to major faults ($R = -0.48$, p-value = 0.14) and distance to major active faults ($R = -0.54$, p-value = 0.08). This co-correlation is due to basins in the Daxue Shan (e.g., wbo445, wbo647) that have high K, high precipitation rates, and are close to active faults. It is possible that these basins are affected by both high precipitation rates and pervasive fault damage.

The correlations between erosion coefficients and mean annual precipitation in different basin groups were mostly non-significant (Table S7). All statistically significant correlations with mean precipitation rates were negative and lower than those with the distance to major faults, except for the one positive correlation with K from plutonic rocks explained earlier. The weak, negative correlation between K and mean annual precipitation in all basins or basins dominated by siliciclastic sedimentary rocks is likely due to the presence of basins in the hinterland that have high K and are close to major faults but experience low precipitation rates. None of the rate constants show statistically significant correlations with *NDVI*. There are positive correlations between both K_{nl} and K_{ss} and *PGA*, but these correlations are weaker than those with distance to major faults.

We also perform multiple stepwise regressions to explain K using five variables (i.e., distance to major faults, distance to major active faults, *MAP*, *NDVI*, and *PGA*). The linear model based on negative relationships with distance to major active faults and mean annual precipitation rates is the best-fit linear model ($F = 8.02$, p-value = 0.0055). If we exclude distance to major active faults due to the similarity between D_{mf} and distance to major active faults, the linear model based on negative relationships with the distance to major faults and mean annual precipitation rates is the best-fit linear model (F = 7.96, p-value = 0.0057). These results are consistent with previous analyses which identified individual correlations, which support strong correlations between erosion coefficients and distance to major faults or distance to major active faults among potential controls.

In summary, our analysis shows that distance to faults is an important control on various erosion coefficients. The similar statistical results from active faults and all faults implies that all faults, regardless of whether they are inactive or active, may have an influence on erosion due to accumulated rock damage over time. The weak or statistically insignificant correlations between erosion coefficients and mean annual precipitation rates indicate that the influence of mean annual precipitation rates in these areas is likely secondary, although we cannot completely rule out the potential influence of precipitation rate or variability in this area (Scherler et al., 2017).

Second, we performed *t*-tests to examine whether the mean values of erosion coefficient, K, are different for several basin groups divided by distance to major faults or lithologic type. We examined the five basin groups of all basins, small basins, and small basins dominated by siliciclastic sedimentary, mixed composition sedimentary, and plutonic rocks. Our null hypothesis is that erosion coefficients from two groups come from independent random samples with normal distributions, equal means, and unequal and unknown variances. We first examined what ranges of distance to major faults produce statistically different K values by comparing mean K from basins at certain intervals of distance to major faults. We examine the intervals of distance from 10 km to 40 km with a 5 km increment. Due to the limited number of samples, all basins (n =111), small basins with A < 200 km^2 (n = 95), and small basins composed of 50% (n = 56) siliciclastic sedimentary have more than 10 samples in 10-km-distance groups (e.g., 0 – 10 km, 10 – 20 km) whereas the other basin groups (those grouped by other lithologies) do not. With a 10 km interval, statistically different mean K values are observed between 0 – 10 km and 10 – 20 km for small basins composed of 50% siliciclastic sedimentary rock. With an interval of 15 km, all basins, small basins with A < 200 km^2, and the small basins composed of 50% siliciclastic sedimentary show statistically different mean K values between 0 – 15 km and 15 – 30 km and similar K values between 15 – 30 km and 30 – 45 km. These three basin groups show statistically different mean K values consistently when examining the intervals of distance from 15 km (e.g., 0 – 15 km vs 15 – 30 km) to 40 km (e.g., 0 – 40 km vs 40 – 80 km). This is likely due to the fact that 74% of K values higher than 1.5×10^{-6} m$^{0.1}$ yr^{-1} are within ~15 km of major faults. Thus, we use 15 km as the cut-off to examine the impact of distance to major faults on K.

Based on this 15 km distance, we perform a second 2-sample t-test for K values from basins within 15 km ($D_{mf} \leq$ 15 km) and greater than 15 km (D_{mf} > 15 km) from major faults. We found that mean K from basins with $D_{mf} \leq$ 15 km are ~2 times higher than those with D_{mf} > 15 km (Tables S8 and S9). Increased mean K is also observed in five basin groups between basins D_{mf} >15 km and $D_{mf} \leq$ 15 km, including all basins (1.9 ± 0.3 (2 s.d.) times), small basins (1.7 ± 0.4 times), and small basins dominated by siliciclastic sedimentary (2.3 ± 0.6 times), mixed composition sedimentary (1.6 ± 0.8 times), and plutonic rocks (1.9 ± 1.0 times) (Fig. 3). In addition, both the all basins and small basins with A < 200 km^2 groupings have statistically significant higher (1.5 to 1.8 times) K values for $D_{mf} \leq$ 15 km compared to those with D_{mf} > 15 km when considering (1) basins sampled before 2008 and (2) basins sampled before 2008 or sampled after the 2008 Wenchuan earthquake outside of the 2008 Wenchuan earthquake severe shaking area (PGA < 0.34 g) (Table S9). This is consistent with observations that do not consider the 2008 Wenchuan earthquake, which implies the observed impact of D_{mf} on K was not due to the bias from samples affected by coseismic landslides from the 2008 Wenchuan earthquake.

Interestingly, we find that mean K from basins with $D_{mf} \leq$ 15 km are higher for basins dominated by siliciclastic sedimentary rock (*ss*) than those dominated by plutonic rocks (*p*). However, there are no differences in mean K between basins with A < 200 km^2 and D_{mf} > 15 km dominated by different lithologic groups including siliciclastic sedimentary (*ss*), mixed composition (*mx*), and plutonic (*p*) rock. This indicates that fault damage in eastern Tibet may potentially induce differences in K depending on lithology with sedimentary rocks experiencing greater fault damage than plutonic rocks.

Lastly, we used an F-test to test whether the model prediction between erosion rates (E) and channel steepness (k_{sn}) is improved when considering (1) different groups of lithology, (2) distance to major faults, and (3) both. Based on equation 3 and n =1, we considered the reduced model of $E = K \cdot k_{sn}$ assuming a single erosion coefficient K. We examined whether the model with more variables (e.g., distance to major faults, lithologies) had a statistically significant improvement compared to the reduced model (Snedecor and Cochran, 1989; Young and Hilley, 2018). The F-statistic for comparing the models is calculated with the following equation:

$$F = \frac{\frac{SSE_1 - SSE_2}{df_1 - df_2}}{\frac{SSE_2}{df_2}} \quad (5)$$

where SSE is the sum of squared errors and df is the degrees of freedom. The subscript 1 and 2 represent the reduced and full model, respectively. The p-values were determined using the numerator degrees of freedom ($df_1 - df_2$) and the denominator degrees of freedom (df_2). If the p-value of the F-statistic ($F_{df_1-df_2,df_2}$) is less than 0.05, we can assume that the full model is a statistically significant improvement compared to reduced model.

First, we compared the reduced model with the full model with different K values from basins dominated by different lithologic groups. We used basins with A < 200 km^2 dominated by siliciclastic sedimentary (*ss*), mixed composition sedimentary (*mx*), and plutonic (*p*) rock. In this case, the full model with different lithologic groups does not show a significant improvement compared to the reduced model of a single K for those basins ($F_{2,82} = 0.61$ with p-value=0.55). Second, we compared the reduced model of a single K with the full model with K that linearly varies with distance to the major faults, D, (e.g., $E = (K_1 \cdot D + K_2) \cdot k_{sn}$). In this case, the full model considering D shows a statistically significant improvement compared to the reduced model ($F_{1,83} = 9.14$ with p-value = 3×10^{-3}). Third, we evaluated the reduced model in which K linearly varies with D compared to the full model in which the variations of K with D are different for each lithologic group (e.g., $E = (K_{i1} \cdot D + K_{i2}) \cdot k_{sn}$ where i = *ss, mx,* and *p*). We find no statistically significant improvements for these groups ($F_{4,79} = 1.87$ with p-value = 0.12). In summary, the model prediction between erosion rates (E) and channel steepness (k_{sn}) is significantly improved when we consider K varying with distance to major faults. However, the model prediction is not improved when we consider K varying with different lithologic groups (plutonic, siliciclastic sedimentary, and mixed composition sedimentary rocks) or with fault distance separately for different lithologic groups. The lack of model improvement for different lithologic groups may imply that the impact of fault damage is more pronounced than lithologic variations in eastern

Tibet. In fact, according to *t*-tests in the previous section, K from different lithologic groups are similar to each other at D_{mf} >15 km. Within D_{mf} of 15 km, K from basins dominated by plutonic and siliciclastic sedimentary rocks differ. However, the small number of plutonic rocks may preclude a significant impact on the *F*-test.

In summary, the results of statistical analyses including observed significant, inverse correlations between distance to major faults and various erosion coefficients, statistically different mean K between basins less than and greater than 15 km from major faults, and a statistically improved model of erosion rates considering channel steepness (k_{sn}) and distance to major faults (D_{mf}), indicate the robust impact of fault damage on erosion and topography in eastern Tibet.

Schmidt Hammer Measurements of Rock Strengths

We measured Schmidt hammer rebound values, hereafter *H*-values, which represent rock hardness or strength at eight sites in eastern Tibet (Figs. S10-S11) (Aydin and Basu, 2005). We used the N-type Proceq Original Schmidt hammer. According to the manufacturer, *H*-values from 25 to 55 correspond to compressive strengths from 14 to 59 MPa on a cylinder with 6 in bore and 12 in stroke (www.proceq.com/). For each site, we made between 30 and 50 measurements with typical equal distance spacings of 0.3 – 1 m.

Of the eight measurement sites, two were located close to the Longmen Shan region (1 in the Pengguan metamorphic complex; 1 in Silurian folded strata). The other 6 measurements were from near the Huya fault in the Min Shan region, which includes two measurements taken in areas containing Permian limestone and four measurements taken in areas containing mixed composition sedimentary rocks including sandstone, phyllite, and interbedded limestone.

All eight sites are within 15 km of major faults. We show the average and 2 s.d. of all measurements and rock type descriptions from each location in Table S10 and show the spread of the data using box plots in Fig. S11. The Pengguan metamorphic complex site has an *H*-value of 48 ± 18 (2 s.d.). The two sites composed of carbonate rocks (Permian limestone) have *H*-values of 44 ± 19 and 53 ± 10. The five locations where we obtain measurements for mixed composition sedimentary rock have values of 24 ± 24, 30 ± 22, 26 ± 23, 26 ± 21, and 24 ± 15. All values from measurements taken on mixed composition sedimentary rocks lie within two standard deviations of each other. The results of Schmidt hammer *H*-values indicate that the mean, median, and maximum values from the metamorphic rock site and carbonate rock sites are higher than those from mixed composition sedimentary rock sites. Since we have not calibrated our *H*-values with the compressive or tensile rock strength measurements in the laboratory (e.g., Murphy et al., 2016), our measured *H*-values should be considered to represent the relative strengths of rocks at these sites.

Supplementary References:

Allen, C.R., Zhouli, L, Hong, Q., Xueze, W., Huawei, Z., and Weishi, H., 1991, Field study of a highly active fault zone: The Xianshuihe fault of southwestern China: Geological Society of America Bulletin, v. 103, p.1178–1199, doi:10.1016/j.quageo.2007.12.001.

Ansberque, C., Godard, V., Bellier, O., Sigoyer, J.D., Liu-Zeng, Xu, X. Ren, Z., Li, Y., and A.S.T.E.R. Team, 2015, Denudation pattern across the Longriba fault system and implications for the geomorphological evolution of the eastern Tibetan margin: Geomorphology, v. 246, p. 542–557, doi:10.1016/j.geomorph.2015.07.017.

Aydin, A., and Basu, A., 2005, The Schmidt hammer in rock material characterization: Engineering Geology, v.81, no.1, p. 1-14.

Balco, G., Stone, J.O., Lifton, N.A., and Dunai, T.J., 2008, A complete and easily accessible means of calculating surface exposure ages or erosion rates from ^{10}Be and ^{26}Al measurements: Quaternary Geochronology, v. 3, p. 174–195, doi:10.1016/j.quageo.2007.12.001.

Bierman, P. and Steig, E.J., 1996, Estimating rates of denudation using cosmogenic abundances in sediment: Earth Surface Processes and Landforms, v. 21, p. 125–139.

Bookhagen, B, and Burbank, D.W., 2010, Toward a complete Himalayan hydrologic budget: Spatiotemporal distribution of snowmelt and rainfall and their impact on river discharge: Journal of Geophysical Research, v. 115, F03019, p. 1-25, doi:10.1029/2009JF001426.

Burchfiel, B.C., and Chen, Z., 2013, Tectonics of the Southeastern Tibetan Plateau and Its Adjacent Foreland: Geological Society of America Special Paper 210, 164 p. doi:10.1130/MEM210

Burchfiel, B.C., Zhiliang, C., Yupinc, L., and Royden, L.H., 1995, Tectonics of the Longmen Shan and Adjacent Regions, Central China Tectonics of the Longmen Shan and Adjacent Regions, Central China: International Geology Review, v. 37, no. 8, p.661–735, doi: 10.1080/00206819509465424.

Chevalier, M.-L., Leloup, P.H., Replumaz, A., Pan, J., Liu, D., Li, H, Gourbet, L, and Métois, M., 2016. Tectonic-geomorphology of the Litang fault system, SE Tibetan Plateau, and implication for regional seismic hazard: Tectonophysics, v. 682, p. 278-292. doi: 10.1016/j.tecto.2016.05.039.

Chen, S. F., and Wilson, C. J. L., 1996. Emplacement of the Longmen Shan Thrust-Nappe Belt along the eastern margin of the Tibetan Plateau: Journal of Structural Geology, v. 18, no. 4,

p. 413–430. doi: 10.1016/0191-8141(95)00096-V.

Chen, S.F., Wilson, C.J.L, Deng, Q.D., Zhao, X.L., and Luo, Z.L., 1994, Active faulting and block movement associated with large earthquakes in the Min Shan and Longmen Mountains, northeastern Tibetan Platea: Journal of Geophysical Research, v. 99, no. B12, p. 24025–24038.

Didan, K., 2015. MOD13Q1 MODIS/Terra Vegetation Indices 16-Day L3 Global 250m SIN Grid V006. NASA EOSDIS Land Processes DAAC. (accessed 2019-08-29 from https://search.earthdata.nasa.gov)

Dunai, P.T., 2010. Cosmic ray-produced radionuclides in Earth Sciences Primary Nature: High-energy charged particles: Cambridge, Cambridge University Press, 14 p.

de Ferranti, J.: Digital elevatiroon data, Url: http://www. viewfinderpanoramas.org/dem3.html, accessed on 18 October 2018.

Finlayson, D.P., Montgomery, D.R., Hallet, B., 2002. Spatial coincidence of rapid inferred erosion with young metamorphic massifs in the Himalayas: Geology, v. 30, no. 3, p. 219-222.

Godard, V., Lave, J. Carcaillet, J., Cattin, R., Bourles, D., and Zhu J., 2010, Spatial distribution of denudation in Eastern Tibet and regressive erosion of plateau margins: Tectonophysics, v. 491. p. 253–274. doi:10.1016/j.tecto.2009.10.026.

Granger, D.E., Kirchner, J.W., Finkel, R., 1996. Spatially Averaged Long-Term Erosion Rates Measured from in Situ-Produced Cosmogenic Nuclides in Alluvial Sediment, The Journal of Geology v. 104, p. 249-257.

Hallet, B. and Hunter, L., 1996, Rates of erosion and sediment evacuation by glaciers: A review of field data and their implication: Global and Planetary Change, v. 12, p. 213–235.

Hartmann, J. and Moosdorf, N., 2012, The new global lithological map database GLiM: A representation of rock properties at the Earth surface: Geochemistry, Geophysics, Geosystems, v. 13, no. 12, p. 1–37.

International Seismological Centre, 2019, ISC-GEM Earthquake Catalogue: https://doi.org/10.31905/d808b825.

Kirby, E. and Ouimet, W.B., 2011, Tectonic geomorphology along the eastern margin of Tibet: insights into the pattern and processes of active deformation adjacent to the Sichuan Basin: Geological Society, London, Special Publications, v. 353, no. 1, p.165–188, doi:10.1144/SP353.9.

Kirby, E., Reiners, P.W., Krol, M.A., Whipple, K.X., Hodges, K.V., Farley, K.A., Tang, W., Chen, Z., 2002. Late Cenozoic evolution of the eastern margin of the Tibetan Plateau: Inferences from $^{40}Ar/^{39}Ar$ and (U-Th)/He thermochronology: Tectonics, v. 21, no. 1001, p. 1-20.

Kirby, E., Whipple, K.X., Burchfiel, B.C., Tang, W., Berger, G., Sun, Z., and Chen, Z., 2000, Neotectonics of the Min Shan: Implications for mechanisms driving Quaternary deformation along the eastern margin of the Tibetan Plateau: Geologic Society of America Bulletin, v. 112, no. 3, p. 375–393, doi:10.1144/SP353.9.

Lal, D., 1991, Cosmic ray labeling of erosion surfaces: in situ nuclide production rates and erosion models: Earth and Planetary Science Letters, v. 104, p. 424–439.

Li, G., West, A.J., Densmore, A., Jin, Z., Zhang, F., Wang, J., Clark, M., and Hilton, R.G., 2017, Earthquakes drive focused denudation along a tectonically active mountain front: Earth and Planetary Science Letters, v. 472, p. 253-265.

Lifton, N., Sato, T., and Dunai, T.J., 2014, Scaling *in situ* cosmogenic nuclide production rates using analytical approximations to atmospheric cosmic-ray fluxes: Earth and Planetary Science Letters, v. 386, p. 149-160.

Long, F., Wen, X.Z., Ruan, X., Zhao, M., and Yi, G.X., 2015. A more accurate relocation of the 2013 M_s7.0 Lushan, Sichuan, China, earthquake sequence, and the seismogenic structure analysis: Journal of Seismology, v. 19, p. 653-665. doi: 10.1007/s10950-015-9485-0.

Montgomergy, D.R., and Brandon, M.T., 2002. Topographic controls on erosion rates in tectonically active mountain ranges: Earth and Planetary Science Letters, v. 201, p. 481-489.

Murphy, B.P., Johnson J.P.L., Gasparini, N.M., and Sklar L.S., 2016. Chemical weathering as a mechanism for the climatic control of bedrock river incision: Nature, v. 532, p. 223-227.

Niemi, N.A., Oskin, M., Burbank, D.W., Heimsath, A.M., and Gabet, E.J., 2005. Effects of bedrock landslides on cosmogenically determined erosion rates: Earth and Planetary Science Letters, v. 237, p. 480–498.

Nishiizumi, K., Imamura, M., Caffee, M.W., 2007, Absolute calibration of ^{10}Be AMS standards: Beam Interactions with Materials & Atoms, v. 258. p. 403-413, doi: 10.1016/j.nimb.2007.01.297

Ouimet, W.B., Whipple, K.X., and Granger, D.E., 2009. Beyond threshold hillslopes: Channel adjustment to base-level fall in tectonically active mountain ranges: Geology, v. 37, no. 7, p. 579–582, doi: 10.1130/G30013A.1.

Pan, G., Ding, J., Yao, D., Wang, L., Luo J., Yan Y., Yong, Y., Zheng, J., Liang, X., Qin, D., Jiang, X., Wang, Q., Li, R., Geng, Q., Liao, Z., and Zhu, D., 2004, Geological map of the Qinghai-Tibet Plateau and adjacent areas: Chengdu Map Publishing House, scale 1:1,500,000, 6 sheets.

Perron, J.T. and Royden, L., 2013, An integral approach to bedrock river profile analysis: Earth Surface Processes and Landforms, v. 38, p.570–576, doi: 10.1002/esp.3302.

Portenga, E. and Bierman, P. R., 2011, Understanding Earth's Eroding Surface with ^{10}Be. GSA Today. v. 21(8), p. 4-10. doi:10.1130/G111A.1

Ren, J., Xu, X., Yeats, R.S., and Zhang, S., 2013a. Latest Quaternary paleoseismology and slip rates on the Longriba fault zone, eastern Tibet: Implications for fault behavior and strain partioning: Tectonics, v. 32, no. 2, p. 216-238. doi: 10.1002/tect.20029.

Ren, J., Xu, X., Yeats, R.S., Zhang, S., Ding, R., and Gong, Z., 2013b. Holocene paleoearthquakes of the Maoergai fault, eastern Tibet: Tectonophysics, v. 590, p. 121-135. doi: 10.1016/j.tecto.2013.01.017.

Ren, J., Xu, X., Zhang, S., Yeats, R.S., Chen, J., Zhu, A., and Liu, S., 2018. Surface rupture of the 1933 M 7.5 Diexi earthquake in eastern Tibet: implications for seismogenic tectonics: Geophysical Journal International, v. 212, p. 1627-1644. doi: 10.1093/gji/ggx498.

Scherler, D., Dibiase, R.A., Fisher, G.B., and Avouac, J.-P., 2017, Testing monsoonal controls on bedrock river incision in the Himalaya and Eastern Tibet with a stochastic-threshold stream power model: Journal of Geophysical Research: Earth Surface, v. 122, p. 1389–1429, doi:10.1002/2016JF004011.

Snedecor, G.W. and Cochran, W.G., 1989, Statistical Methods: Ames, Iowa, Iowa State University Press.

Schwanghart, W. and Scherler, D., 2014. Short Communication: TopoToolbox 2 – MATLAB-based software for topographic analysis and modeling in Earth surface sciences: Earth Surface Dynamics, v. 2, p.1–7, doi:10.5194/esurf-2-1-2014.

Stone, J.O., 2000. Air pressure and cosmogenic isotope production: Journal of Geological

Society of London, v. 105, no. B10, p.753–759.

Taylor, M. and Yin, A., 2009. Active structures of the Himalayan-Tibetan orogen and their relationships to earthquake distribution, contemporary strain field, and Cenozoic volcanism: Geosphere, v. 5, no. 3, p.199–214. doi: 10.1130/GES00217.1.

Tian, Y., Li, R., Tang, Y, Xu, X, Wang, Y, and Zhang, P., 2018. Thermochronological constraints on the late Cenozoic morphotectonic evolution of the Min Shan, the eastern margin of the Tibetan Plateau: Tectonics. v. 37, no. 6, p. 1733-1749, doi:10.1029/2017TC004868.

U.S. Geological Survey, 2017, ShakeMap – Earthquake Ground Motion and Shaking Intensity Maps: U.S. Geological Survey, doi: 10.5066/F7W957B2.

Wang, E., Kirby, E., Furlong, K.P., van Soest, M., Xu, G., Shi, X., Kamp, P.J.J., and Hodges, K.V., 2012. Two-phase growth of high topography in eastern Tibet during the Cenozoic: Nature Geoscience, v. 5, p. 640-645. doi: 10.1038/NGEO1538.

West, A.J., Hetzel, R., Li, G., Jin, Z., Zhang, F., Hilton, R.G., and Densmore, A.L., 2014. Dilution of ^{10}Be in detrital quartz by earthquake-induced landslides: Implications for determining denudation rates and potential to provide insights into landslide sediment dynamics: Earth and Planetary Science Letters, v. 396, p. 143-153.

Whipple, K.X. and Tucker, G.E., 1999, Dynamics of the stream-power river incision model: Implications for height limits of mountain ranges, landscape response timescales, and research needs: Journal of Geophysical Research, v. 104, no. B8, p. 17661-17674.

Wobus, C., Whipple, K.X., Kirby, E., Snyder, N., Johnson, J., Spyropolou, K., Crosby, B., and Sheehan, D., 2006, Tectonics from topography: Procedures, promise,and pitfalls, *in* Willett, S.D., Hovius, N., Brandon, M.T., and Fisher, D.M., eds., Tectonics, Climate, and Landscape

Evolution: Geological Society of America Special Paper 398, Penrose Conference Series, p. 55–74, doi: 10.1130/2006.2398(04).

Xu, X., Gao, R., Guo, X., Li, W., Li, H., Wang, H., Huang, X, and Lu, Z., 2017, Outlining tectonic inheritance and construction of the Min Shan region, eastern Tibet, using crustal geometry: Scientific Reports, v. 7, no.13798, p.1–8, doi:10.1038/s41598-017-14354-4.

Xu, C., Xu, X., Yao, X., Dai, F., 2014, Three (nearly) complete inventories of landslides triggered by the May 12, 2008 Wenchuan Mw 7.9 earthquake of China and their spatial distribution statistical analysis: Landslides, v. 11, p. 441–461, doi:10.1007/s10346-013-0404-6.

Yan, D.-P., Qiu, L., Wells, M.L., Zhou, M.-F., Meng, X., Lu, S., Zhang, S., Wang, Y., and Li, S.-B., 2018. Structural and Geochronological Constraints on the Early Mesozoic North Longmen Shan Thrust Belt: Foreland Fold-Thrust Propogation of the SW Qinling Orogenic Belt, Northeastern Tibetan Plateau: Tectonics, v. 37, no. 12, p. 4595-4624. doi: 10.1029/2018TC004986.

Yan, D.-P., Zhou, M.-F., Li, S.-B., and Wei, G.-Q., 2011. Structural and geochronological constraints on the Mesozoic-Cenozoic tectonic evolution of the Longmen Shan thrust belt, eastern Tibetan Plateau: Tectonics, v. 30, TC6005, p. 1-24. doi: 10.1029/2011TC002867.

Young, H.H., and Hilley, G.E., 2018, -scale denudation rates of the Santa Lucia Mountains, California: Implications for landscape evolution in steep, high-relief, coastal mountain ranges: Geological Society of America Bulletin. v. 130, no. 11-12, p. 1809-1824. doi:10.1130/B31907.1.

Zhang, Y., Replumaz, A., Leloup, P.H., Wang, G., Bernet, M., van der Beek, P., Paquette, J.L. and Chevalier, M., 2017, Cooling history of the Gongga batholith: Implications for the

Xianshuihe Fault and Miocene kinematics of SE Tibet: Earth and Planetary Science Letters, v. 465, p. 1–15, doi:10.1016/j.epsl.2017.02.025.

Zhang, Y.-Z., Replummaz, A., Wang, G.-C., Leloup, P.H., Gautheron, C., Bernet, M., van der Beek, P., Paquette, J.L., Wang, A., Zhang, K.-X., Chevalier, M.-L., and Li, H.-B., 2015. Timing and rate of exhumation along the Litang fault system, implication for fault reorganization in Southeast Tibet: Tectonics, v. 34, p. 1219-1243. doi: 10.1002/ 2014TC003671.

B. Supplementary figures

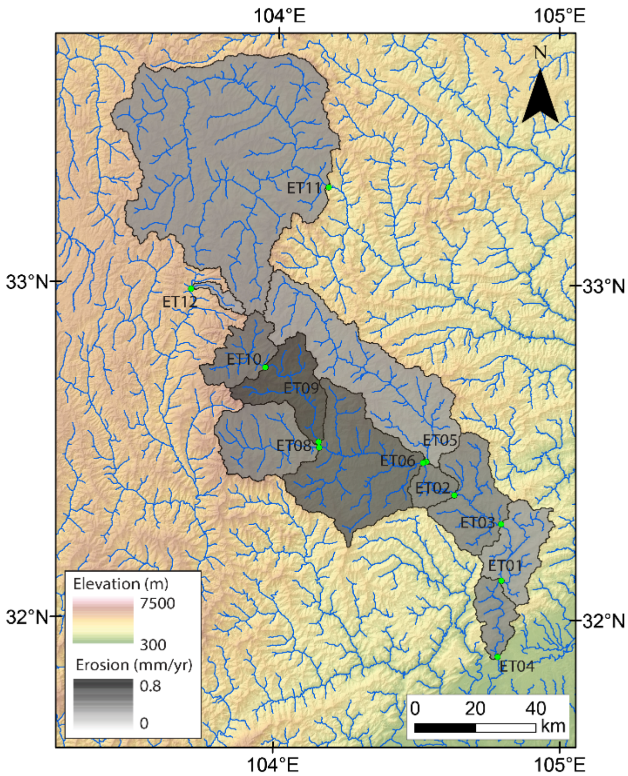

Figure S1. Elevation map of the Min Shan area with the 11 new sample collection sites and basin outlines from this study. Sample names are shown in black, channel networks are shown in blue, and sample collection sites are shown with green dots. Note that all samples except for ET05, 08, 10-12 have nested basins. Erosion rates from basins which are not from nested basins are shown on top of those which are from nested basins.

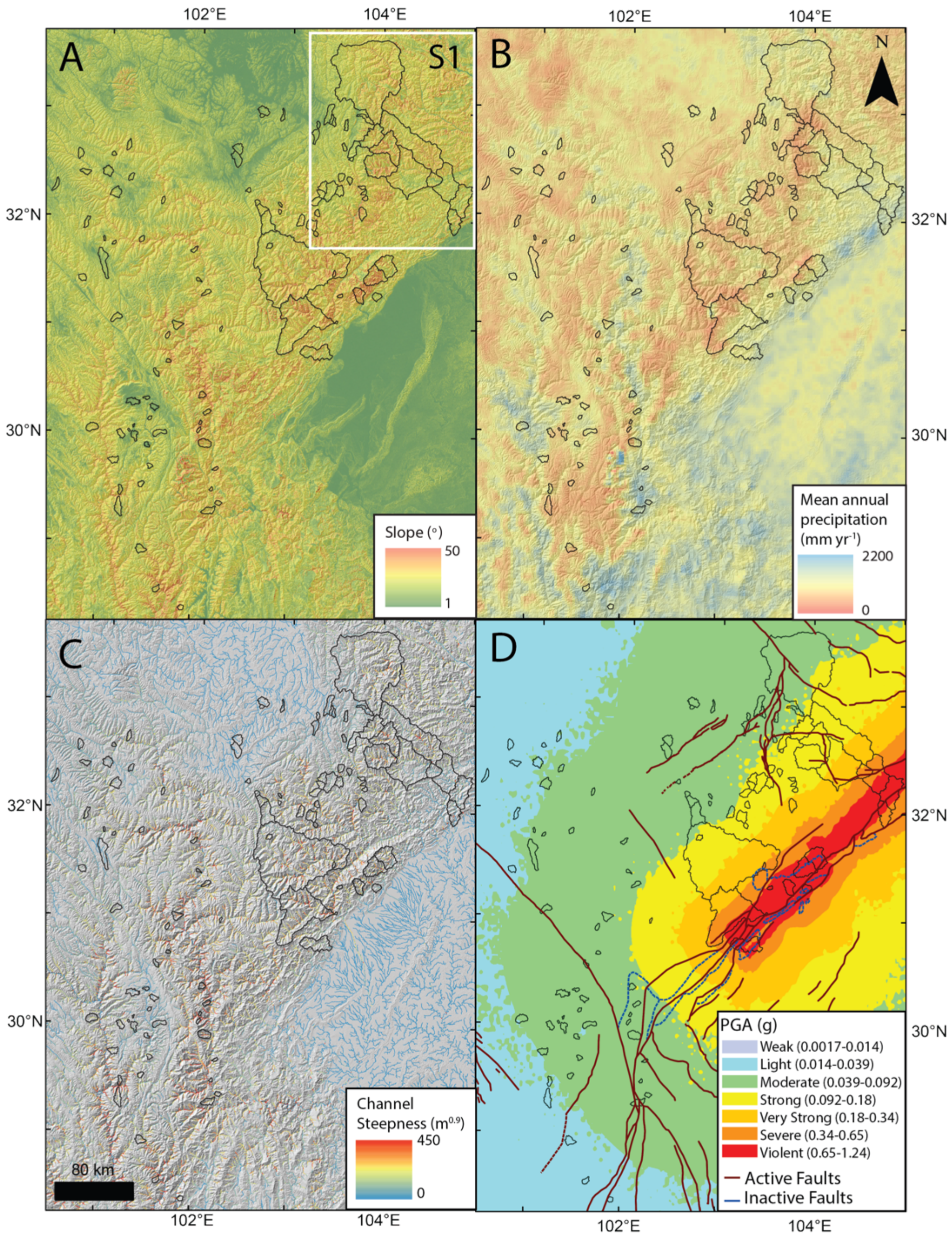

Figure S2. Maps showing (A) slope, (B) mean annual precipitation from Bookhagen and Burbank (2010), and (C) channel steepness shown for channel sections with drainage areas larger than 10 km^2 in eastern Tibet, and (D) peak ground acceleration (*PGA*) from the 2008 Wenchuan earthquake (from USGS ShakeMap v4). Black outlines represent all basins compiled from previous studies and measured in this study. A white box in (A) represents the area shown in Fig. S1.

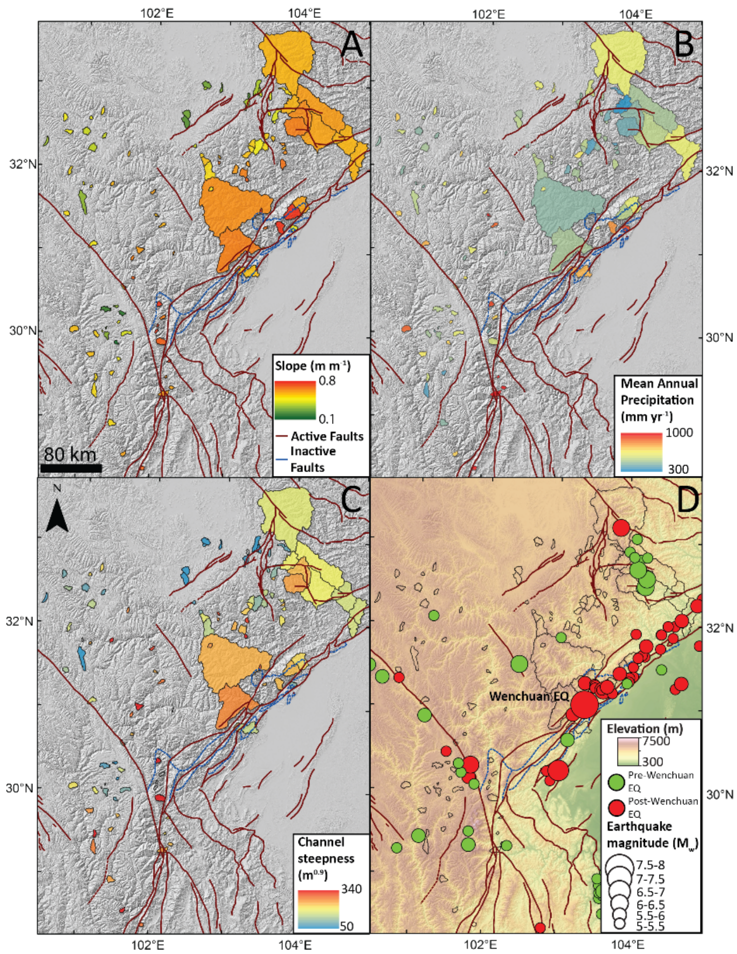

Figure S3. Maps showing basin-averaged (A) slope, (B) mean annual precipitation from Bookhagen and Burbank (2010), and (C) channel steepness from the integral method in eastern Tibet. (D) Elevation map with earthquakes from M_w 5 to 8 with larger circles showing higher magnitude earthquakes. Earthquakes before the 2008 Wenchuan earthquake are shown with green circles and those after the 2008 Wenchuan earthquake are shown with red circles. Earthquakes shown in the compilation occurred from 1970 through July 2018. Earthquakes were retrieved from www.iris.edu.

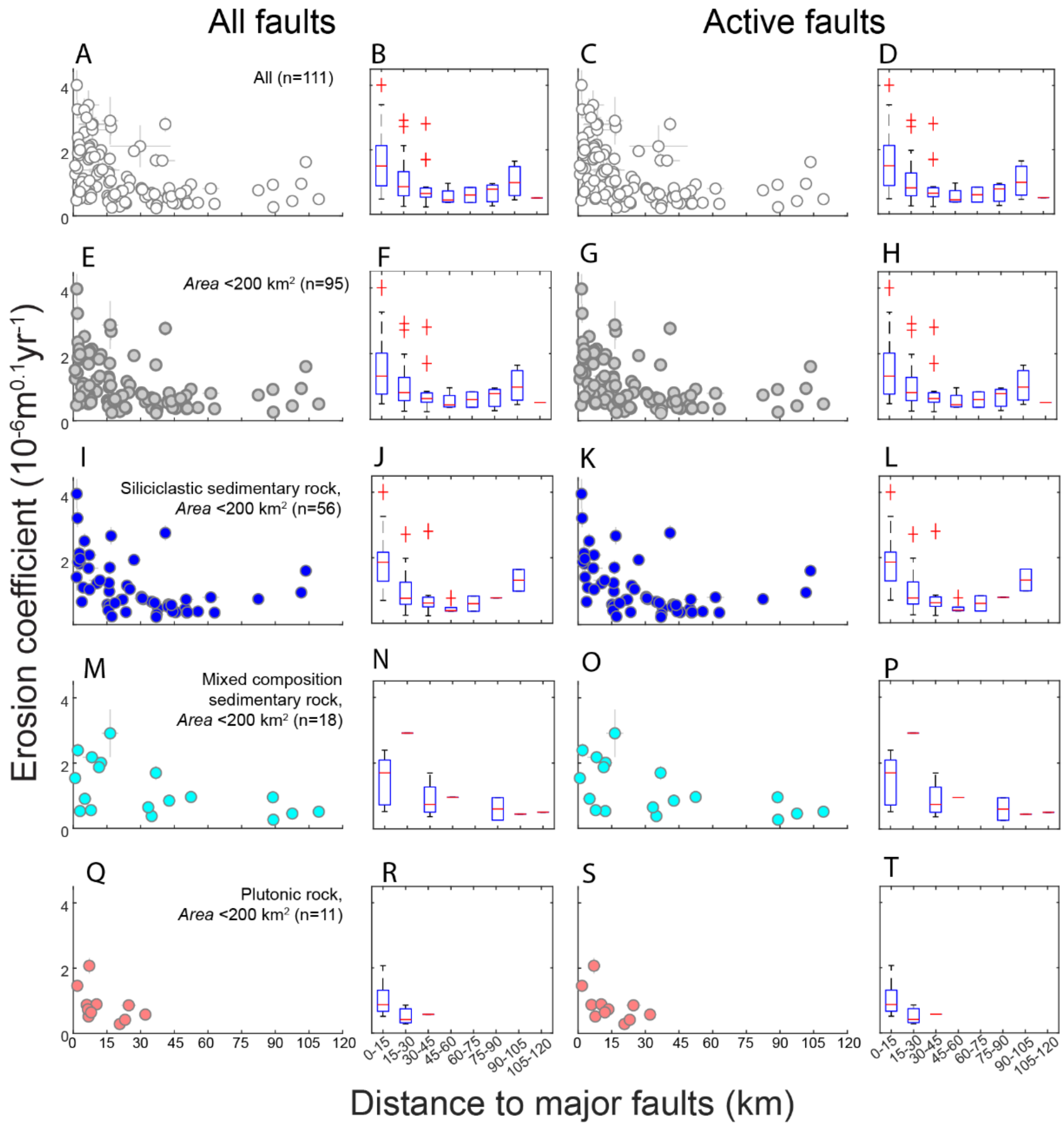

Figure S4. Scatter plots (A, C, E, G, I, K, M, O, Q, S) and box plots (B, D, F, H, J, L, N, P, R, T) showing how erosion coefficients vary with (A, B, E, F, I, J, M, N, Q, R) the distance to major faults and (C, D, G, H, K, L, O, P, S, T) distance to major active faults for A-D) all basins, E-H) small basins with area < 200 km^2, and small basins dominated by I-L) siliciclastic sedimentary rock, M-P) mixed composition sedimentary rock, and Q-T) plutonic rock. All basins, small basins, and small basins dominated by siliciclastic sedimentary, mixed composition sedimentary, and plutonic rocks are shown in circles with white, gray, blue, cyan, and salmon colors, respectively in the scatter plots. The top and bottom of the blue sides of the box plots show the 25th and 75th percentiles, respectively. The central red mark in the box shows the median. The whiskers show the extent of data within 99.3%, and red crosses show outliers.

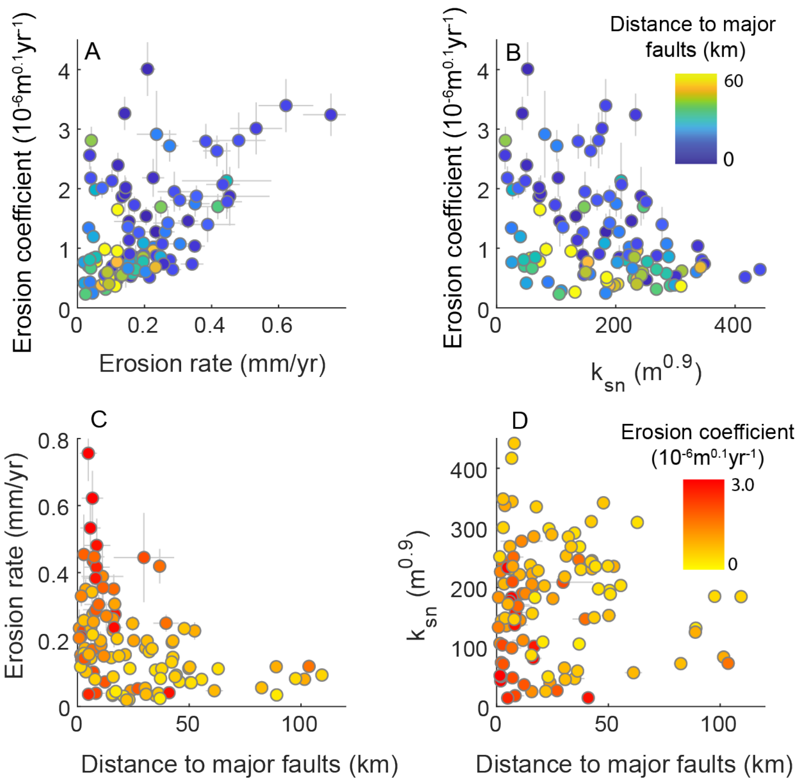

Figure S5. Scatter plots showing erosion coefficient vs. (A) erosion rate and (B) channel steepness (k_{sn}), color-coded for distance to major faults, and distance to major faults vs (C) erosion rate and (D) channel steepness (k_{sn}), color-coded for erosion coefficient. The control of distance to major faults on erosion coefficients is observed in a wide range of erosion rates and k_{sn} values.

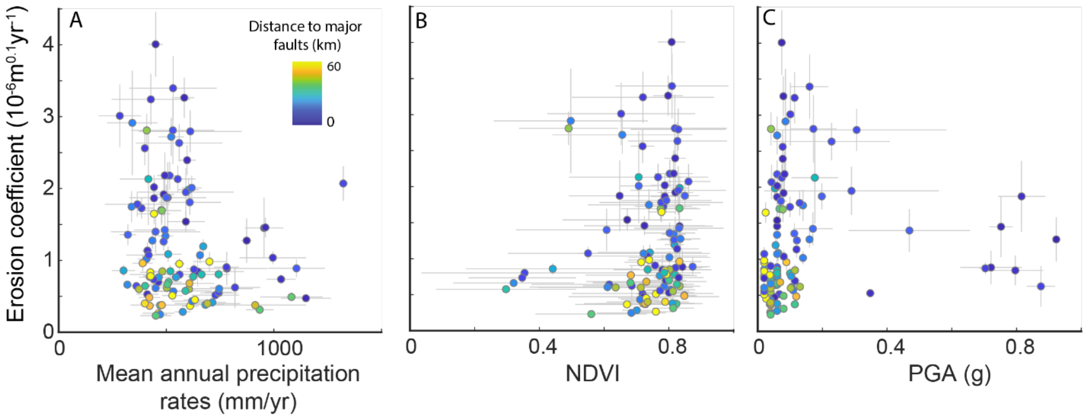

Figure S6. Relationships between basin-averaged erosion coefficient and (A) basin-averaged mean annual precipitation rates, (B) basin-averaged *NDVI*, and (C) peak ground acceleration (*PGA*) from the 2008 Wenchuan earthquake from all basins in this study. The colors represent distance to major faults.

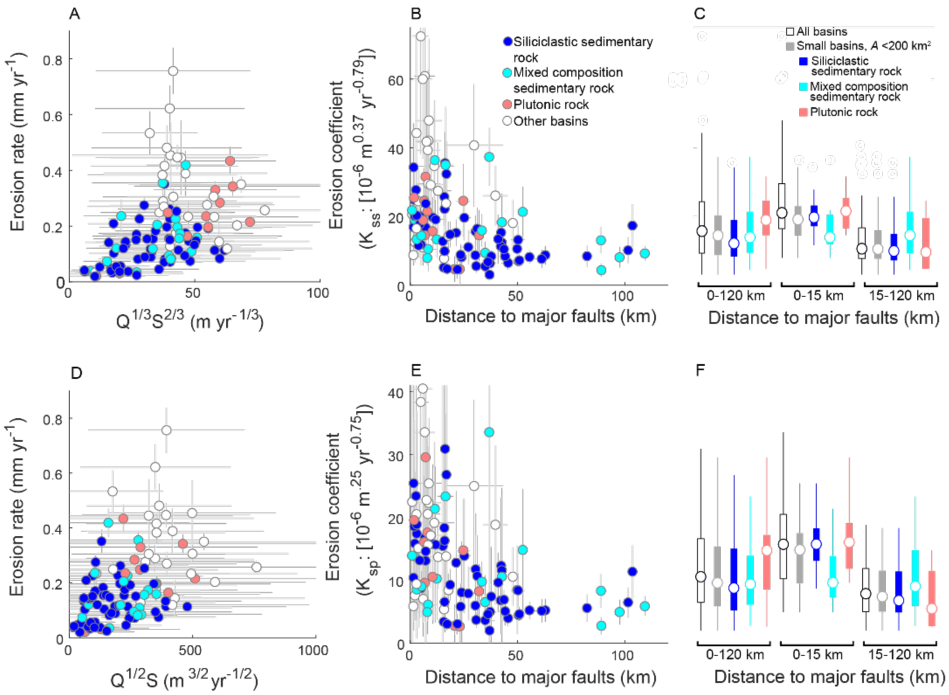

Figure S7. Plots of (A, D) erosion rates vs. the product of discharge and slope and (B,C,E,F) erosion coefficients vs. distance to major faults, color-coded for small basins dominated by different lithologic groups. Erosion coefficients K_{ss} and K_{sp} are based on river incision models assuming A-C) shear stress and D-F) stream power, respectively. Symbols are the same as in Fig. 3.

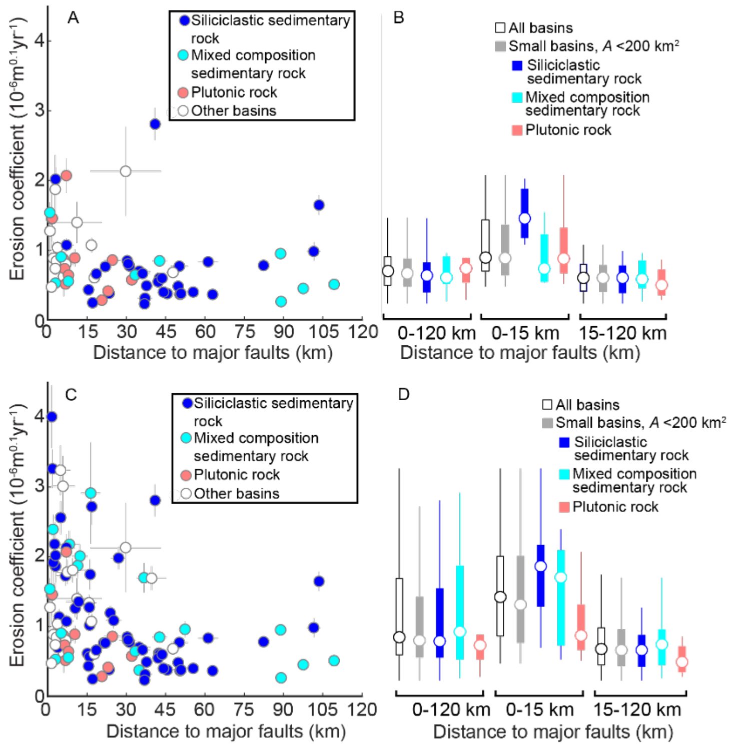

Figure S8. A,C) Erosion coefficient versus distance to major faults, color-coded for small basins dominated by different lithologic groups. B,D) Boxplots showing erosion coefficient ranges from different lithologies separated by distances to major faults. The plots show results from A,B) samples collected before the 2008 Wenchuan earthquake and C,D) samples collected before and after the 2008 Wenchuan earthquake but outside of the severe shaking range (*PGA* < 0.34 g). Symbols are the same as in Fig. 3. In both cases, we see that both the all basins grouping and the small basins grouping for D_{mf} ≤15 km have ~1.5 to 1.8 times higher erosion coefficients than those basins with D_{mf} >15 km.

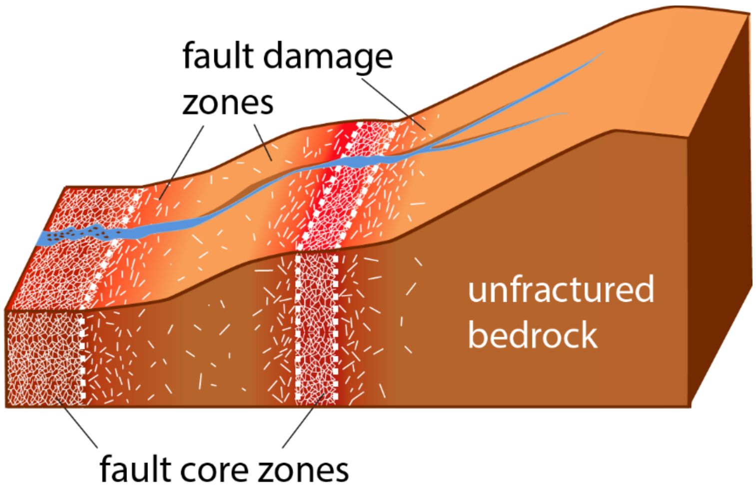

Figure S9. Conceptual diagram of fault core and damage zones and idealized topographic expression. Rock strength increase from fault core zones (e.g., gauge, cataclasite) to fault damage zones (e.g., jointed or fractured rocks) to unfractured intact bedrock. The topographic slope near the fault zone is gentler due to greater rock damage. Map not to scale.

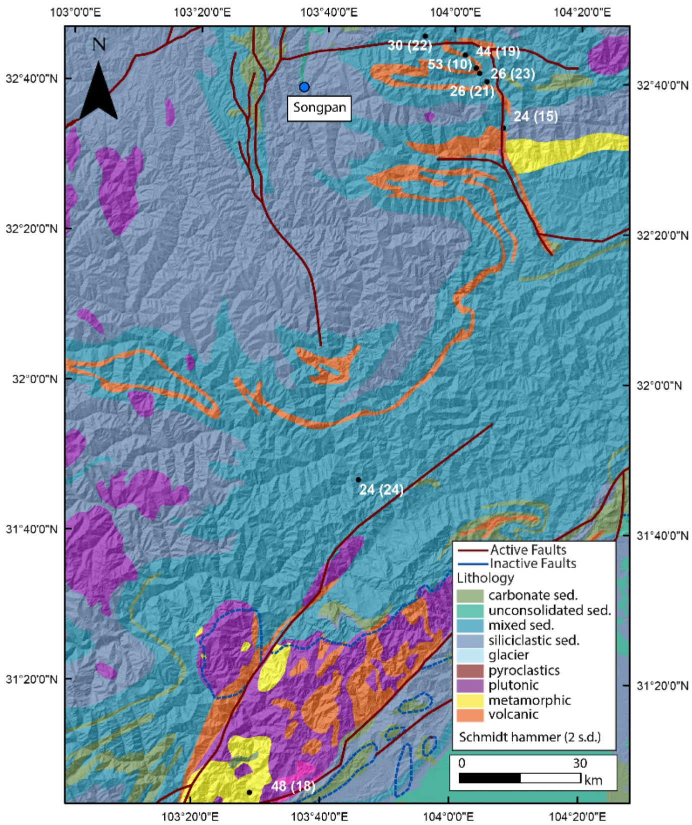

Figure S10. Lithology of the northeastern Longmen Shan and Min Shan area (Hartmann and Moosdorf, 2012) with the locations of Schmidt hammer measurements shown in black dots. The numbers in white are the average Schmidt hammer rebound values, and those in parenthesis show two standard deviation values. Brown lines show the active faults and blue lines shown inactive faults compiled in this study. The blue dot shows the location of the city of Songpan.

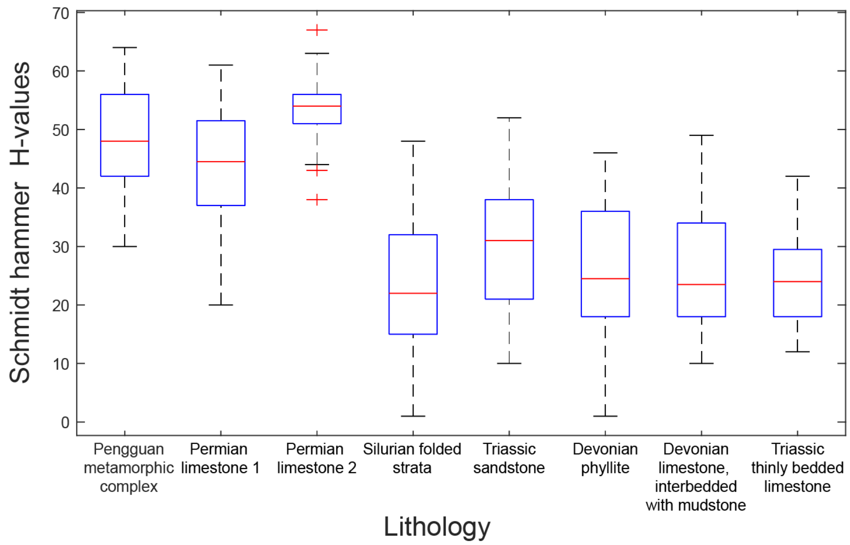

Figure S11. Boxplots showing the ranges of Schmidt hammer rebound values (*H*-values) for 8 sites. The top and bottom of the blue sides of the box show the 25th and 75th percentiles, respectively. The central red mark shows the median. The whiskers show the extent of data within 99.3%, and red crosses show outliers.

C. Supplementary tables

Please see the attached excel file.